

Lipid Droplets Embedded in a Model Cell Membrane Create a Phospholipid Diffusion Barrier

Sevde Puza, Stefanie Caesar, Chetan Poojari, Michael Jung, Ralf Seemann, Jochen S. Hub, Bianca Schrul, and Jean-Baptiste Fleury*

Lipid droplets (LDs) are ubiquitous, cytoplasmic fat storage organelles that originate from the endoplasmic reticulum (ER) membrane. They are composed of a core of neutral lipids surrounded by a phospholipid monolayer. Proteins embedded into this monolayer membrane adopt a monotopic topology and are crucial for regulated lipid storage and consumption. A key question is, which collective properties of protein-intrinsic and lipid-mediated features determine spatio-temporal protein partitioning between phospholipid bilayer and LD monolayer membranes. To address this question, a freestanding phospholipid bilayer with physiological lipidic composition is produced using microfluidics and micrometer-sized LDs are dispersed around the bilayer that spontaneously insert into the bilayer. Using confocal microscopy, the 3D geometry of the reconstituted LDs is determined with high spatial resolution. The micrometer-sized bilayer-embedded LDs present a characteristic lens shape that obeys predictions from equilibrium wetting theory. Fluorescence recovery after photobleaching measurements reveals the existence of a phospholipid diffusion barrier at the monolayer–bilayer interface. Coarse-grained molecular dynamics simulation reveals lipid specific density distributions along the pore rim, which may rationalize the diffusion barrier. The lipid diffusion barrier between the LD covering monolayer and the bilayer may be a key phenomenon influencing protein partitioning between the ER membrane and LDs in living cells.

1. Introduction


Lipid droplets (LDs) are cytoplasmic organelles specialized for the storage of metabolic energy in the form of neutral lipids such as triglycerides and sterol esters.^[1,2] They originate from

the endoplasmic reticulum (ER) membrane where neutral lipids are synthesized. While the molecular mechanisms of this process are unknown, it appears that LD biogenesis is following a three-stage process: neutral lipid synthesis, lens formation (via intra-membrane lipid accumulation), and finally LD formation.^[3] At relatively low concentrations, neutral lipids accumulate between the two leaflets of the ER bilayer to eventually form a lipid reservoir with a lens shape.^[3,4] Numerical modeling suggests that such lenses could exist in the ER membrane with a size of tens of nanometers.^[3,5,6] Upon the continuous production of neutral lipids, they accumulate into the reservoir which leads to a lipid lens growth. Above a certain size, this lipid lens becomes unstable and can lead to a spontaneous budding of the oily reservoir.^[3,7] Ultimately, the droplet pinch-off from the membrane leads to its release into the cytosol.^[8–10]

LDs dynamically adapt to metabolic changes in the cell and balance uptake of free fatty acids by their esterification and storage as triglycerides, and consumption of triglycerides by the release of fatty acids

under catabolic conditions. These essential metabolic functions of LDs are executed by proteins on the LD surface, many of which dynamically partition from the ER bilayer to the LD monolayer membrane.^[11,12] Aberrant LD functions are implicated in numerous metabolic diseases such as obesity, diabetes,

S. Puza, M. Jung, R. Seemann, J.-B. Fleury
Saarland University
Experimental Physics and Center for Biophysics (ZBP)
Saarland University
66123 Saarbrücken, Germany
E-mail: jean-baptiste.fleury@physik.uni-saarland.de

 The ORCID identification number(s) for the author(s) of this article can be found under <https://doi.org/10.1002/smll.202106524>.

© 2022 The Authors. Small published by Wiley-VCH GmbH. This is an open access article under the terms of the Creative Commons Attribution-NonCommercial-NoDerivs License, which permits use and distribution in any medium, provided the original work is properly cited, the use is non-commercial and no modifications or adaptations are made.

S. Caesar, B. Schrul
Medical Biochemistry and Molecular Biology
Center for Molecular Signaling (PZMS)
Faculty of Medicine
Saarland University
66421 Homburg, Germany

C. Poojari, J. S. Hub
Saarland University
Theoretical Physics and Center for Biophysics (ZBP)
Saarland University
66123 Saarbrücken, Germany

DOI: 10.1002/smll.202106524

or cardiovascular disorders.^[13] It is therefore key to unravel the protein-intrinsic and lipid-mediated mechanisms underlying LD biogenesis, including the spatio-temporal protein partitioning between phospholipid bilayer and LD monolayer membranes.

In cells, LDs appear to be spherical via microscopy investigation. The LD diameters range between 0.1 and 5 μm in many cells, but the diameter may also exceed 100 μm in certain cells.^[14] The LD surface is covered by a phospholipid monolayer that includes phosphatidylcholine (PC), phosphatidylethanolamine (PE), cholesterol, and many other biomolecules and proteins.^[14–18] No transmembrane proteins have been identified on LDs yet,^[11] which is in line with the hypothesis that exposure of soluble domains into the hydrophobic neural lipid core is energetically unfavored and that a monotopic protein topology is a prerequisite to allow proteins to partition from a bilayer membrane to the LD surface.

In this article, we report the existence of a diffusion barrier that may play an important role in the spatial organization of proteins between the LD and the bilayer. We produced a microfluidic 3D-chip from a combination of soft lithography and micro-machining^[19] that allowed us to fabricate a horizontal, free-standing, stable, fluid and solvent-free lipid bilayer.^[20] We dispersed LDs with an average diameter of $\approx 5 \mu\text{m}$ around this free-standing bilayer and, depending on its molecular composition,

the LDs can be inserted spontaneously into the bilayer core within a few minutes. Using confocal microscopy, we measured the 3D-shape of the reconstituted LDs for different bilayer tensions. The different bilayer tensions are monitored by tuning the cholesterol concentration of the bilayer. The bilayer-embedded LDs exhibited a symmetric lens shape. However, if we reconstituted proteins in the LDs, the bilayer-embedded LDs exhibited an asymmetric shape. Based on wetting theory, we demonstrate that both the symmetric and the asymmetric LD shapes correspond to equilibrium states.^[21] Conducting fluorescence recovery after photobleaching (FRAP) measurements on the LD surface, we obtained a reduced exchange rate of PE, and PC, phospholipids between the surface of the LDs and the bilayer. This indicates that LDs produce a diffusion barrier, which restrains the lateral motility of phospholipids, with putative effects on the distribution of membrane proteins.^[22]

2. Results and Discussion

2.1. Lipid Bilayer Characterization

We developed a 3D-microchip that enables the formation of a free-standing horizontal lipid bilayer at a desired position

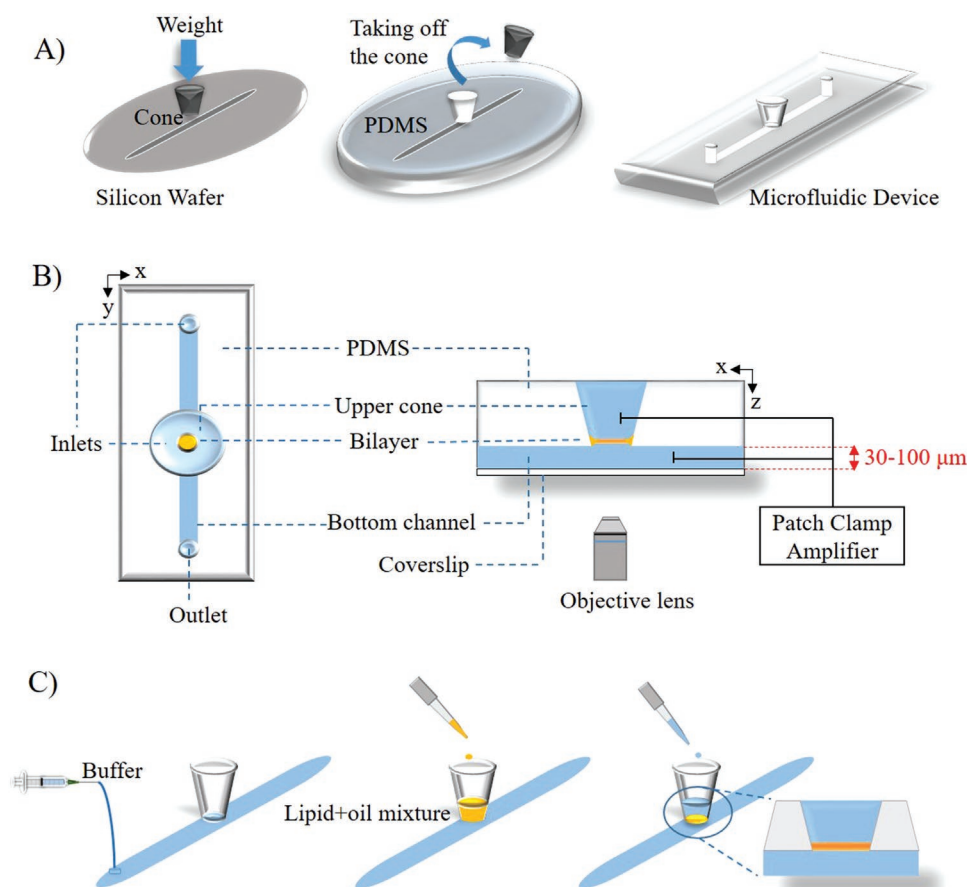


Figure 1. Schematic of the microfluidic device fabrication and operation. A) A micro-machined aluminium cone is combined with a bottom channel on a silicon wafer, which is produced by classical photolithography techniques. PDMS is cast around this mold and cross linked, removed from the mold, and closed by bonding the PDMS to a glass cover-slip. The thus build system consists of a two layer microfluidic device with one bottom channel combined with an upper conical reservoir. B) 3D scheme of the formed microchip filled with liquids. C) Fabrication of the lipid bilayer. The free standing bilayer forms between upper cone and bottom reservoir and is easy to control by the upper cone that is open toward air.

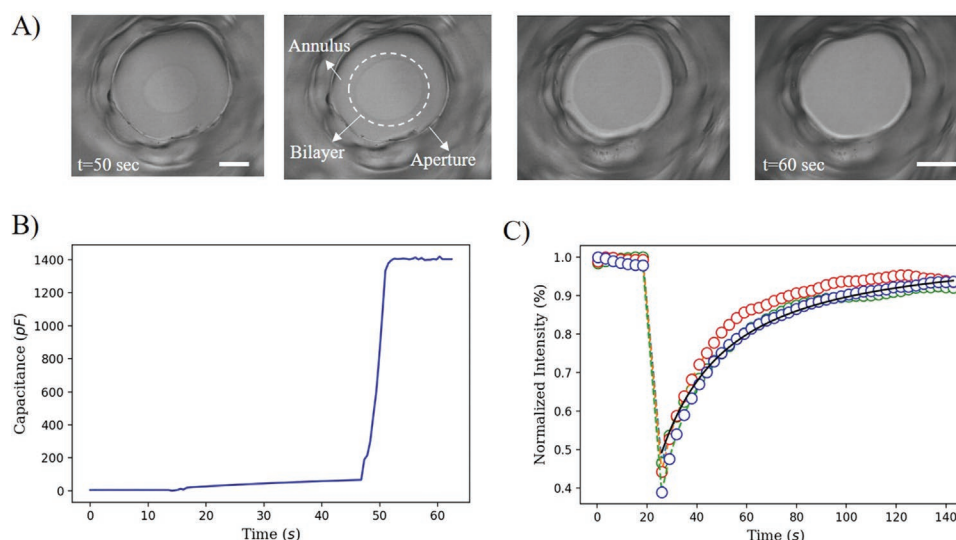


Figure 2. A) Optical microscopy time series showing the bilayer formation after adding lipid oil mixture and a second buffer drop via the conical opening of the device. A bilayer starts to form in the middle of the aperture and grows until it covers the entire aperture area. Scale bar shows 200 μm . B) Capacitance measurement of the bilayer formation by patch clamp recordings. The capacitance value is very low right after adding the liquids and jumps with first visible circular bilayer, then increases as long as the bilayer grows. C) Three experimental FRAP curves of lipid bilayer are presented with the dots; the Soumpasis fit to one data set is represented by the black line.

(see **Figure 1**), similar to other platforms reported in the literature.^[20,23,24] However, our chip allows a superior optical access due to the reduced optical distance between the glass bottom of the microfluidic device and the formed bilayer (between 30 and 100 μm , **Figure 1**).^[20,23,24] Moreover, and in contrast to previous systems, this platform enables to measure quantitatively the phospholipid fluidity on LD via FRAP.^[25]

To form a bilayer, the bottom channel of the microfluidic device is filled with buffer (**Figure 1C**). Then the oily phase ($\approx 4 \mu\text{L}$ squalene) containing the dissolved phospholipids is deposited with a micro pipette directly into the cone, and subsequently, a second buffer droplet ($\approx 10 \mu\text{L}$) is also deposited with a micro-pipette into the cone. This droplet is sliding down the conical opening and spreads on the previously deposited oil layer. Thus, the chip contains two water buffer phases separated by an oil–lipid layer (**Figure 1B**). The lipids (1,2-dioleoyl-sn-glycero-3-phosphocholine (DOPC), 1,2-dioleoyl-sn-glycero-3-phosphoethanolamine (DOPE), 1,2-dioleoyl-sn-glycero-3-phospho-L-serine (sodium salt) (DOPS)) dissolved in the oil phase decorate the two oil–water interfaces with a monolayer within a short time. As the microfluidic device material (PDMS) is porous, the oily phase initially separating the two water–oil interfaces is automatically drained into the PDMS. During this oil drainage, the two water–oil interfaces that are covered by a lipid monolayer, are brought into contact and produce a bilayer within ≈ 10 –20 min. The formation of this bilayer is simultaneously monitored by optical bright-field microscopy (**Figure 2A**) and electrically by capacitance measurement (**Figure 2B**). Optically, a tiny disk briefly appears in the center of the oil–water sandwich (**Figure 2A**). A few seconds later, a bright and sharp ring suddenly appears around this growing disk-like area indicating the formation and expansion of a lipid bilayer. The bright ring spreads further outward and disappears when it coincides with the edge of the hole. The corresponding area expansion and final bilayer formation is confirmed by

simultaneous capacitance measurements (**Figure 2B**). Initially, the measured capacitance C is negligible, which confirms that the two water–oil interfaces are at fairly large distance. Exactly, when the tiny disk appears in bright-field microscopy, the capacitance signal C increases at $t \approx 47$ s (**Figure 2B**) until reaching a stable plateau, at $t \approx 52$ s, indicating that the bilayer expansion has reached the limits of the microfluidic hole. The associated specific capacitance per area, $C/A \approx 0.01 \text{ F/m}^2$, is in line with literature values of oil-free lipid bilayers.^[20,26] If not stated otherwise, we used the bilayer composition of DOPC/DOPE/DOPE (60:10:30) throughout this study, representing a reasonable model for the lipid composition of the ER membrane.^[27]

2.2. LDs and Proteo-LDs Insertion

After the lipid bilayer formation, we dispersed artificial LDs in the buffer phase with a reasonable composition compared to the available literature.^[14–18] Such LDs consist of triolein droplet coated with a phospholipid monolayer.^[14–18] Adding BODIPY to the LD core, a fluorescent sensor for neutral lipid,^[28] the core of LDs becomes visible with fluorescence microscopy. It enables to characterize the LDs size and to observe their diffusion in bulk. The average LD size is approximately 5 μm , suggesting via the Einstein relation a diffusion coefficient in the order of $0.1 \mu\text{m}^2 \text{ s}^{-1}$.^[29] To test the bio-relevance of our setup, we also generated LDs that contain monolayer-integrated hairpin proteins as they are present on LDs in living cells. To this end, we reconstituted the hairpin-region-containing peptide of the LD hairpin protein (UBXD8) into LDs, which we refer to as proteo-LDs (PLDs). The size of proteo-PLDs is typically around 15 μm due to a slightly different preparation routine (see Experimental Section). The estimated diffusion coefficient is $\approx 0.033 \mu\text{m}^2 \text{ s}^{-1}$.^[29] The LDs and PLDs diffuse freely in the buffer phase, until they eventually reached the lipid bilayer. Once an LD (or PLD) touches

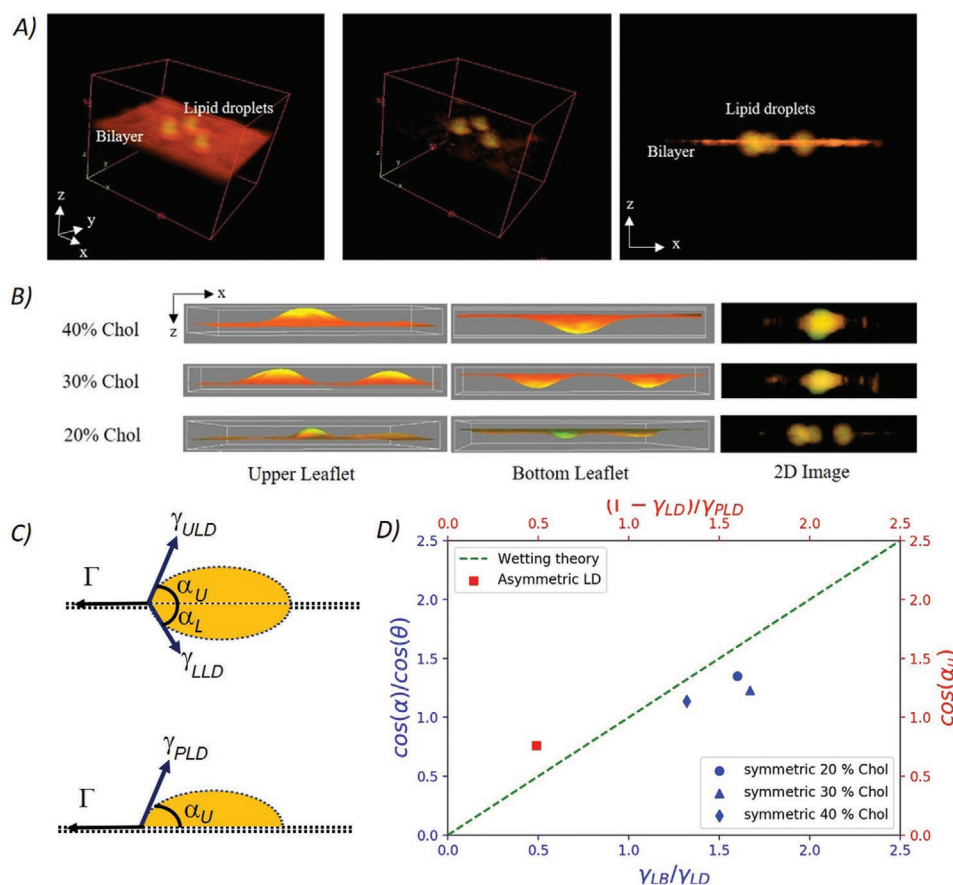


Figure 3. A) 3D and 2D-projected confocal micrographs of a lipid bilayer and LDs embedded inside. The phospholipids are visible in red (ATTO-DOPE) and the core of the LDs is visible in greenish yellow (BODIPY). Scale bars with arrows for the 3D images are 10 μm for x, y, and z, and for the 2D image 10 and 2 μm for x and z. B) Quasi 2D surface plot projections of 3D reconstructed upper sides and lower sides of LD droplets as function of cholesterol concentration in the lipid bilayer (left and middle row), and examples of 2D-projected LDs for corresponding concentrations. Scale bars are 5 μm and 200 nm for x and z (left two rows) and 5 and 2 μm for x and z (right row). C) Scheme of a LD geometry embedded into the bilayer denoting the action of the bilayer tension Γ , of the LD monolayer tensions γ , and of the LD contact angles α . D) Comparison between wetting theory and the force balance extracted from the symmetric LD 3D-geometry and the measured surface tension (blue axis). The case of asymmetric PLDs and the asymmetric wetting theory is presented in the red axis.

the bilayer, it can insert into the bilayer core forming an inclusion with a characteristic shape^[30] and stops moving. Thus, a moving LD or PLD can be considered as freely diffusing in the bulk, while an immobile LD (or PLD) can be considered as inserted into the bilayer core. Having two dyes with different emission signals, one for the lipid droplet core (BODIPY) and one for the phospholipid (Atto-DOPE), we could confirm the successful insertion of LDs inside the bilayer (Figure 3A). In particular, the BODIPY signal is only visible at the position of the LD position and no BODIPY signals could be observed in the bilayer otherwise.

Interestingly, LDs (or PLD) only coated with PC phospholipids do not insert rapidly (not before one hour) into the bilayer. To investigate the conditions of LD insertion, we produced LDs that are coated with a mixture of PC:PE (1:1 molar ratio) and also dispersed these LDs around the bilayer. After 10–15 min, we observed a spontaneous insertion of several of these LDs into the bilayer, demonstrating that the presence of PE in the LD surface significantly reduces the insertion energy barrier. These findings are rationalized by the fact that fusion of the LD monolayer with the bilayer likely proceeds via a stalk-like intermediate

state, which exhibits strong negative curvature along the stalk rim. Because the cone-shaped PE lipids favor negative curvature, they may accumulate along the pore rim and, thereby, stabilize the stalk intermediate.^[31,32] Notably, PLDs and LD required the same conditions for successful insertion into the bilayer.

Bleaching the entire area of an embedded LDs, we could erase the entire fluorescent signal from the BODIPY dye without measuring any fluorescent recovery (Supporting Information). This fact confirms that no trace of neutral lipids could be measured inside the core of the lipid bilayer. Moreover, this indicates that all the embedded LDs are isolated from the others LDs, that is, there are no flows, or any other transport of neutral lipids, between the different LDs embedded into our bilayer.

2.3. Wetting of Embedded LDs and Proteo-LDs in a Bilayer

To investigate the wetting properties of LDs and PLDs after insertion into the bilayer, we characterized the 3D-shape of those LDs using high resolution 3D-confocal microscopy imaging.

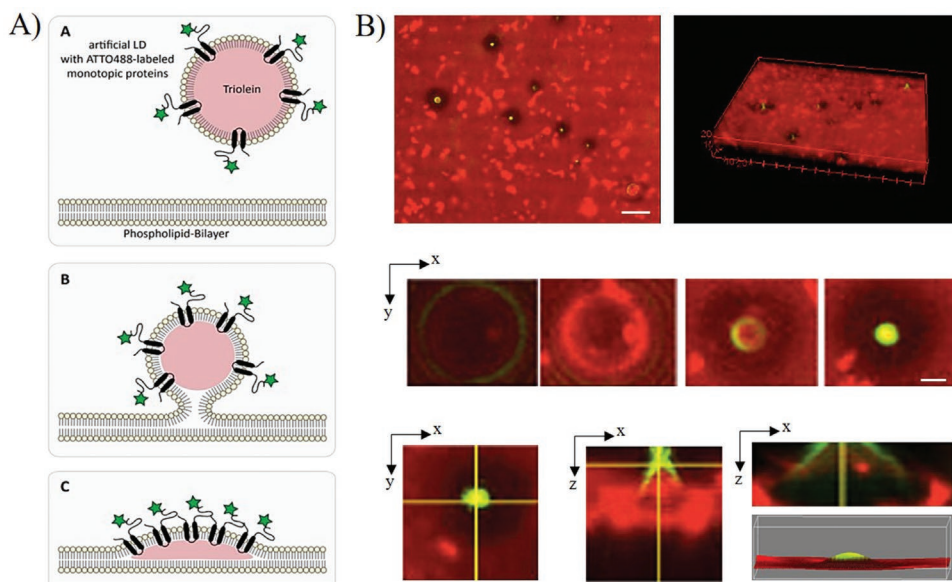


Figure 4. A) Scheme of the PLD insertion pathway. B) Lipid bilayer observed under fluorescence microscopy containing PLDs. The PLDs are labeled with a fluorescent hairpin protein (green signal); the PE bilayer lipids contain 4% fluorescent molecules (red signal, PE-Atto). The core of the PLDs is not fluorescent and thus appears black in the 3D reconstruction of the PLDs (top row), and in the individual micrographs of a z-stack (middle and lower row). The bottom right image shows quasi 2D surface plot projection of a 3D reconstructed PLD. Scale bars (x,y arrows) denote 15 μm for upper two images, and 10 μm for lower two rows of images. Scale bars (z arrows) denote 1 μm and 700 nm for lower middle and right rows of images.

Reconstituted LDs exhibit a symmetric lens shape with a radial dimension in the micrometer range, and a normal extension (perpendicular to the bilayer) of in the micrometer range (Figure 3). PLDs, in contrast, present a highly asymmetric shape bulged towards the protein containing leaflet (see Figure 4).

To vary the wetting properties of the membrane and, thereby, to explore a range of LD lens shapes, we varied the total ratio of cholesterol content of the bilayer. We found that the insertion angle α of the LDs decreases with increasing cholesterol content in the bilayer (from $(49 \pm 3)^\circ$ for 20% cholesterol to $(29 \pm 2)^\circ$ for 40%), while keeping the characteristic symmetric lens shape (Figure 3A,B). To rationalize the dependence of the insertion angles with cholesterol content, we compared the measured 3D-geometry of the LDs with expectations from wetting theory.^[6,33–36] The shape of embedded LDs is defined by the balance between the bilayer tension Γ and the tensions applied by the horizontal components of the LD upper leaflet surface tension $\Gamma_{\text{ULD}} = \gamma_{\text{ULD}} \cdot \cos(\alpha_{\text{U}})$ and the lower leaflet surface tension $\Gamma_{\text{LLD}} = \gamma_{\text{LLD}} \cdot \cos(\alpha_{\text{L}})$ such as:

$$\Gamma = \gamma_{\text{ULD}} \cdot \cos(\alpha_{\text{U}}) + \gamma_{\text{LLD}} \cdot \cos(\alpha_{\text{L}}) \quad (1)$$

where α_{U} and α_{L} are the measured angles as defined in Figure 3C and γ_{ULD} and γ_{LLD} are the surface tensions of the upper and lower leaflet covering the LD. In equilibrium, the bilayer tension is defined by the Young–Dupré law, $\Gamma = 2\gamma_{\text{LB}} \cdot \cos(\theta)$,^[33] where γ_{LB} is the surface tension of a monolayer decorated oil-water interface and 2θ is the contact angle of the plateau border. In case of symmetric bilayer where $\gamma_{\text{ULD}} = \gamma_{\text{LLD}} = \gamma_{\text{LD}}$, we can thus reformulate Equation (1) to

$$\frac{\gamma_{\text{LB}}}{\gamma_{\text{LD}}} = \frac{\cos(\alpha_{\text{U}}) + \cos(\alpha_{\text{L}})}{2\cos(\theta)} \quad (2)$$

As the symmetric bilayer also results in symmetric droplet shapes, we have further $\alpha_{\text{U}} = \alpha_{\text{L}} = \alpha$ (see scheme in Figure 3) and can simplify Equation (2) to

$$\frac{\gamma_{\text{LB}}}{\gamma_{\text{LD}}} = \frac{\cos(\alpha)}{\cos(\theta)} \quad (3)$$

From the independently measured angles α , θ and the measured surface tensions values γ_{LB} , γ_{LD} (see Table 1), we could

Table 1. Physical characterization of a symmetric bilayer. As the phospholipids are diffusing between the LD and the bilayer, even in the presence of the diffusion barrier, the LD monolayer phospholipidic composition will be the same as the bilayer in the long run. Thus, the values reported for the LD composition correspond to a phospholipidic composition that is identical to the bilayer composition.

Chol	LB surface tension γ	LB contact angle 2θ	LB tension Γ	LD tension γ_{LD}	LD angle α
20%	2.9 mN m^{-1}	$(49 \pm 3)^\circ$	3.8 mN m^{-1}	1.74 mN m^{-1}	$(33 \pm 3)^\circ$
30%	3.0 mN m^{-1}	$(41 \pm 3)^\circ$	4.5 mN m^{-1}	1.79 mN m^{-1}	$(27 \pm 2)^\circ$
40%	2.5 mN m^{-1}	$(29 \pm 2)^\circ$	4.3 mN m^{-1}	1.89 mN m^{-1}	$(24 \pm 2)^\circ$

verify that these values satisfy the Equation (3) as plotted in Figure 3D. It results that the measured lens shapes are corresponding to an equilibrium wetting morphology and the reduction of the insertion angle with increasing cholesterol concentration appears to be a consequence of a changed bilayer tension as function of increasing cholesterol concentration, which is consistent with literature.^[37]

Besides, we analyzed the shapes of PLDs inserted into the lipid bilayer core. We measured two different fluorescent signals, one from the labeled proteins in the LD monolayer and one for the phospholipids present inside the bilayer (Figure 4B). The presence of labeled proteins on the bulged surface of the PLD is clearly visible in the series of high-resolution confocal microscopy z-scans. When inspecting the z-stack along the 3D-geometry of PLDs, we can follow the fluorescence signal of the LD-proteins while moving from the starting z-position (here, the bilayer core) to the final z-position (the top of the PLD). At the starting position, we observe a green ring which indicates that the proteins are covering the interface between the bilayer and the PLD. This fluorescent ring shrinks while rising the position of the z-scan. At a z-position of ≈ 700 nm, a large fluorescent spot appears suddenly, which is due to the fact that the PLDs appear quite flat at their top. The optical signal is coming from a large area on top of the PLD and, thus, it is appearing as a fluorescent spot. This demonstrates two important points: first, the monotopic hairpin proteins are present on the PLD surface and accumulate only in the monolayer leaflet from which the PLD inserted into the bilayer. Second, the majority of these proteins are not diffusing into the phospholipid bilayer but stay localized on the PLD monolayer even after 30 min.

As already mentioned above, we observed that all the scanned inserted PLDs do not present a symmetric lens shape but exhibit a clear asymmetric shape, which is typical of a bulged droplet.^[30] This breaking of symmetry is due to the proteins that are coating only one side of the LD and the correspondingly asymmetric surface tension. Consistent with the monotopic hairpin topology, these proteins stay on the monolayer side from which the PLDs insertion occurred. Based on wetting theory,^[33,34] such an asymmetric PLD shape in equilibrium would satisfy the following relation:

$$\Gamma = \gamma_{\text{PLD}} \cdot \cos(\alpha_U) + \gamma_{\text{LD}} \cdot \cos(\alpha_L) \quad (4)$$

with γ_{PLD} being the surface tension of the protein containing the upper leaflet and its contact angle α_U , and γ_{LD} being the surface tension of the bottom leaflet and its contact angle α_L (see scheme in Figure 3C). Due to the fact that the LD is strongly bulging in only one direction and its highly asymmetric shape (Figure 4B), we can assume $\alpha_L \approx 0$ so that $\gamma_{\text{LD}} \cdot \cos(\alpha_L) \approx \gamma_{\text{LD}}$. Thus, we can rewrite Equation (4) as:

$$\frac{\Gamma - \gamma_{\text{LD}}}{\gamma_{\text{PLD}}} = \cos(\alpha_U) \quad (5)$$

From the measured angle α_U and the measured tensions Γ , γ_{LD} , γ_{PLD} , we could verify that these values satisfy Equation (5), as plotted in Figure 3D. Hence, same as the LD shape, the PLD shape is also in equilibrium with respect to the acting surface

tension because the surface tension of the leaflet is altered substantially by the presence of the protein, so the partitioning of a sufficiently large quantity of proteins in the outer leaflet might be able to cause budding of a LD from the bilayer.

2.4. Lipid Diffusion Barrier between LD and a Bilayer

Besides exploring the bilayer-embedded LD shapes in detail, we explored the phospholipid exchange rate at the LD-bilayer interface. First, we investigated the fluidity of the phospholipids composing the bilayer by performing FRAP measurements on the bilayer. The recorded fluorescent recovery curves follow the Soumpasis equation,^[38] demonstrating that the phospholipid molecules are freely diffusing in the bilayer (Figure 5A,C). The extracted coefficient of phospholipid diffusion is $\approx 10 \mu\text{m}^2 \text{s}^{-1}$, which is similar to the diffusion coefficient of phospholipids in giant unilamellar vesicles (GUVs)^[39] or in other free-standing lipid membranes.^[20] This motility is around three to four times faster than the phospholipid motility measured with supported bilayers.^[40]

To measure the exchange rate of phospholipids in the bilayer with the phospholipids in the monolayer that are covering the LD, we produced LDs without fluorescent phospholipids but with the neutral lipid fluorescent sensor, BODIPY. Thus, before reconstitution, the LD neutral lipid core is fluorescently labeled while the phospholipid monolayer covering its surface is not visible under fluorescence excitation. After reconstitution of the LDs into the bilayer, the lipids composing the LD monolayer exchange with the fluorescently labeled phospholipids of the bilayer, which makes the LD visible with time. This means that the phospholipid molecules could exchange from the bilayer to the LD and vice-versa. To quantitatively characterize the phospholipid exchange rate at the bilayer-LD interface, we additionally performed FRAP measurements on the phospholipids present on the entire LD surface. The corresponding results are plotted in Figure 5C and reveal an astonishing diminution of the motility of phospholipids diffusing from the bilayer onto the LD surface. The Soumpasis fit suggests an associated phospholipid diffusion coefficient in the range of $0.1\text{--}0.5 \mu\text{m}^2 \text{s}^{-1}$, corresponding to a decrease of the phospholipid mobility with respect to the bilayer of approximately one order of magnitude, which indicates the presence of a pronounced diffusion barrier at the bilayer-LD interface. However, the diffusion constants from the Soumpasis fit should be considered with care as the Soumpasis equation is not valid in the presence of a diffusion barrier. Nevertheless, we obtained clear evidence of a lipid diffusion barrier at the interface between the LDs and the bilayer while the diffusive motion of the other phospholipid molecules moving anywhere on the bilayer, or on the LDs surface, stay unaffected.

To quantify the phospholipid exchange rate in presence of this diffusion barrier in more detail, we further consider the case of two membranes in contact. Where one membrane contains fluorescent molecules at $t = 0$, and the other membrane does not contain any fluorescent molecules at $t = 0$. At equilibrium, these two membranes could exchange their molecules in a reversible manner. The transport of these fluorescent molecules can be expressed as:

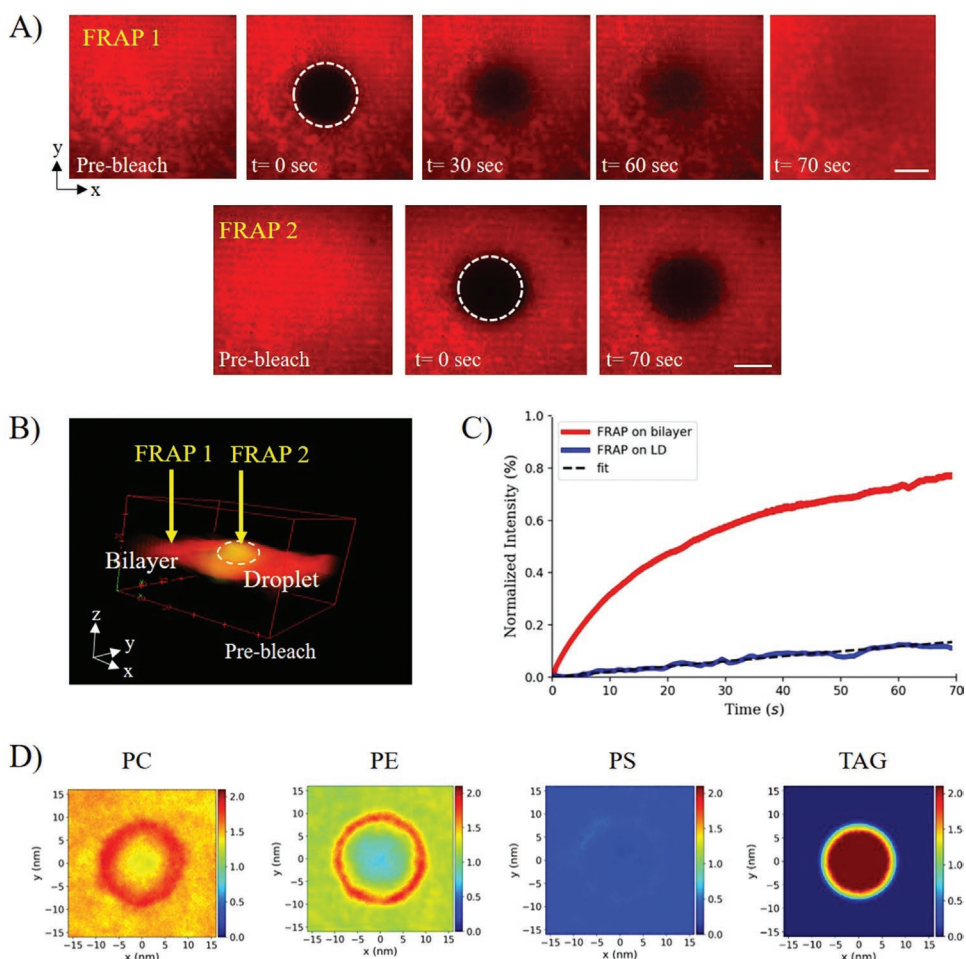


Figure 5. A) FRAP experiments were performed on the bilayer position (FRAP 1), and on the entire LD surface (FRAP 2) as indicated in panel (A). Scale bars are 25 μm (upper panel) and 5 μm (lower panel). B) 3D-representation of a confocal micrograph showing an LD embedded inside a bilayer. The PE bilayer lipids are visible in red (PE-Atto), and the core of the LDs are visible in green (BODIPY). Scale bars with arrows denote 10 μm for x, y, and z directions. C) FRAP data obtained from measurements performed on the bilayer position (FRAP 1), and on the LD entire surface (FRAP 2). The fit of Equation (9) to the data “FRAP 2” gives a transport rate of $k \approx 0.25 \text{ (min}^{-1}\text{)}$. D) Coarse-grained molecular dynamics simulation revealing the lateral lipid densities on an LD monolayer and a surrounding bilayer. For these simulations, the same lipidic compositions were employed as in the experiments (TAG is 537 triacylglycerol, see Experimental Section).

$$[A] \rightleftharpoons [B] \quad (6)$$

where $[A]$ is the concentration of fluorescent phospholipids in the donor membrane and $[B]$ is the concentration of fluorescent phospholipids in the acceptor membrane. From this first order, one stage reversible reaction model, we can define the following differential equation for the fluorescent lipid transfer rate

$$\frac{d[A]}{dt} = -\frac{d[B]}{dt} = k_{-1}[B] - k_1[A] \quad (7)$$

where k_1 , k_{-1} are the corresponding transport rates. With the initial conditions $[A]_{t=0} = N$, $[B]_{t=0} = 0$ and assuming that $k_{-1} = k_1 = k$, we can express the solution of Equation (7) as:

$$[B] = \frac{N}{2}(1 - e^{-2kt}) \quad (8)$$

$$\Delta I = \frac{Na}{2}(1 - e^{-2kt}) \quad (9)$$

where ΔI is the measured change in fluorescence signal, and a is a scaling factor. Fitting the fluorescence recovery data on the totality of the LD surface, which is plotted in Figure 5C, we extracted a transport rate of $k = 0.25 \text{ min}^{-1}$. This value is nearly one order of magnitude lower than the estimated transport rate $k \approx 3 \text{ min}^{-1}$ from the lipids diffusing freely inside the bilayer if we fit the fluorescence recovery of a pure bilayer. The presented results are confirming the diffusion barrier for PE phospholipids.

To test whether the diffusion barrier is specific to PE molecules, or whether it exists similarly for PC phospholipids, we repeated the previous experiments by replacing the fluorescent PE molecules by fluorescent labeled PC molecules (see Experimental Section). The corresponding PC transport rates were found to be similar to the ones measured with the PE

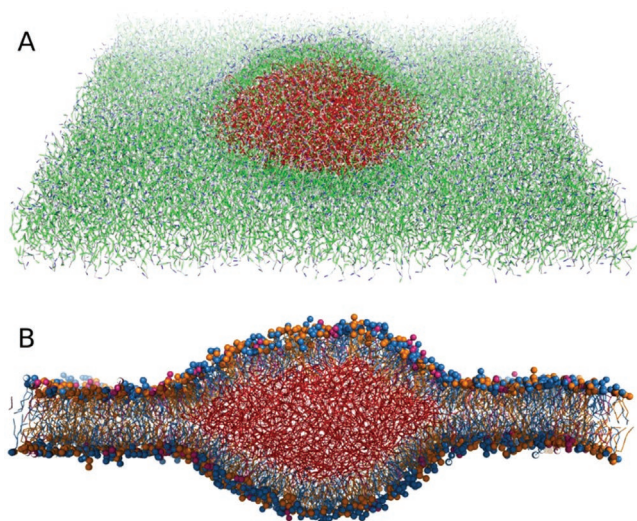


Figure 6. Equilibrated coarse-grained simulation system of an LD. A) Neutral lipids are shown as red sticks and phospholipids as green/blue/white sticks. B) DOPC in blue, DOPE in orange, and DOPS in pink. Water and sodium beads are not shown for clarity.

phospholipids (see Supporting Information), suggesting that this diffusion barrier exists both for PC and PE phospholipids.

In order to identify a possible biophysical origin of this diffusion barrier between phospholipids in a bilayer leaflet and the phospholipids in the monolayer covering a LD, we additionally performed molecular dynamics (MD) simulations of LDs for similar lipid compositions using the coarse-grained MARTINI model (Figure 6).^[41] The simulations revealed that the PE molecules accumulate in a ring structure at the interface between the LD and the bilayer (Figure 5D). This can be rationalized by the fact that the cone-shaped DOPE lipids are capable of stabilizing the negative membrane curvature along the LD rim, in line with recent studies.^[42,43] We thus hypothesize that the accumulation of PE lipids may be a structural source for the diffusion barrier for PC and PE phospholipids. To test whether the MARTINI simulation reproduces the experimentally identified diffusion barrier, we computed the mean first passage times (MFPTs) of PE, PC, and PS lipids between the LD surface and area of the surrounding bilayer. Compared to MFPTs obtained with pure bilayers, the LD–bilayer MFPTs were systematically larger, hence confirming the presence of a diffusion barrier. However, the MFPTs were increased by only 23% to 39%, indicating a much weaker diffusion barrier compared to the

Table 2. Lateral diffusion of lipids from the LD surface to the bilayer in coarse-grained MD simulations as compared to lateral diffusion in a pure-bilayer simulation (see Figure 6), revealing a mild diffusion barrier between LD and bilayer (see Experimental Section). Total number of LD-to-bilayer transitions within approx. 9.5 μs (N_{trans}) and mean first passage time. The last column is the relative increase of the MFPT.

	Pure bilayer simulation		LD simulation		Rel. increase
	N_{trans}	MFPT [μs]	N_{trans}	MFPT [μs]	
DOPC	7346	0.44	2025	0.61	39%
DOPE	5733	0.44	1600	0.54	23%
DOPS	1399	0.45	423	0.57	27%

experimental conditions (see Table 2). The quantitative discrepancy may be rationalized by the different spatial dimensions; the simulations were performed with an LD with a nanometric size, while the experiments were performed with LDs with micrometric size. As nanoscopic regions are more unstable under thermal fluctuation, the observed PE-ring is expected to be more stable and larger for a micrometric LD and, thereby, might enhance the diffusion barrier. In addition to such dimensional effects, we cannot exclude the possibility that the coarse-grained force field underestimates the diffusion barrier.

3. Conclusion

In this article, we revealed the existence of a lipid diffusion barrier at the interface between individual embedded LD and a free-standing bilayer. For this purpose, we produced a free-standing bilayer in a 3D microfluidic chip. Artificial LDs are dispersed near the bilayer and may insert spontaneously into a PC/PE bilayer core within a few minutes provided the LDs are covered by a PC/PE monolayer. Using confocal microscopy, we could demonstrate the LD insertion and determined the geometry of reconstituted LD. It results that the LDs present a characteristic lens shape with a radial and height dimension in the micrometer range. Analyzing the droplet geometry as a function of different surface and thus bilayer tension, we could demonstrate that the lens shape corresponds to an equilibrium wetting geometry. Surface tensions were tuned by varying the cholesterol concentration in the formed bilayer. Interestingly, if the LDs were enriched with proteins before insertion, the bilayer-embedded LDs exhibited an asymmetric shape that results from the asymmetric distribution of the proteins. Despite this asymmetry, we demonstrated that this droplet shape also corresponds to an equilibrium wetting geometry. This fact indicated that the partitioning of a sufficiently large quantity of proteins in a leaflet might be able to cause spontaneous budding of an LD from the bilayer.

In contrast to previous studies, our platform allows to conduct quantitative FRAP measurements on the LDs and the bilayer. We could demonstrate that phospholipids diffuse normally on the bilayer. However, when performing FRAP on the entire bilayer-embedded LD, we could measure an astonishing diminution of the recovery rate resulting from a reduced diffusion of phospholipids coming from the bilayer to the LD monolayer. This demonstrates the existence of a diffusion barrier at the LD–bilayer interface, which restrains the lateral diffusion of phospholipids between these two regions and may affect the distribution of membrane proteins. We measured the existence of this diffusion barrier for PE and PC phospholipids. In order to identify a possible biophysical origin of this diffusion barrier between phospholipids in a bilayer leaflet and the phospholipids in the monolayer covering an LD, we additionally performed molecular dynamics (MD) simulations of LDs for similar lipid compositions using the coarse-grained MARTINI model. The simulations revealed that the PE molecules accumulate in a ring structure at the interface between the LD and the bilayer. This ring structure may be due to the cone-shape of the PE phospholipids that are capable to stabilize the negative curvature along the LD rim. First-mean

passage time in simulations confirm the existence of a diffusion barrier. However, the simulation obtained a reduction of the phospholipid exchange rate by only $\approx 30\%$, while we measured a reduction of this exchange rate that is approximately three times higher in experiments. We suppose that the origin of this difference is due to scale difference between the experimental micrometric LD and the numerical nanoscopic LD. Thus, the PE-ring may be larger, and more stable, in micrometric LD. This diffusion barrier, which restrains the lateral motility of phospholipids, has putative effects on the partitioning of proteins between the endoplasmic reticulum (ER) membrane and LDs in living cells.

We suppose that the microfluidic setup applied for this study can be employed, in the future, also to quantitatively determine protein diffusion and localization within these distinct types of membranes. In particular, it enables the monitoring of the dynamic protein partition, as a function of spatial protein localization on the LD surface, or on the surrounding ER bilayer membrane, respectively. Importantly, our system enables us to modulate various lipid-mediated parameters such as phospholipid packing or surface tension to determine their contribution to bilayer–monolayer protein partitioning.

4. Experimental Section

Materials: Lipids were 1,2-dioleoyl-sn-glycero-3-phosphocholine (DOPC), 1,2-dioleoyl-sn-glycero-3-phosphoethanolamine (DOPE), 1,2-dioleoyl-sn-glycero-3-phospho-L-serine (sodium salt) (DOPS), and cholesterol purchased from Avanti Polar Lipids. Glycerol trioleate (Triolein) and squalene were purchased from Sigma-Aldrich. Fluorescence dyes 4,4-difluoro-1,3,5,7,8-pentamethyl-4-bora-3a,4a-diazas-indacene (BODIPY 493/503, D3922, ThermoFisher), 1,2-dioleoyl-sn-glycero-3-phosphoethanolamine-N-(lissamine rhodamine B sulfonyl) (ammonium salt) (18:1 Liss Rhod PE), 1,2-dioleoyl-sn-glycero-3-phosphocholine-N-(Cyanine 5) (18:1 PC-Cy5), 1,2-Dioleoyl-sn-glycero-3-phosphoethanolamine labeled with Atto 647N (Atto-DOPE) were obtained from Avanti Polar Lipids. For microfluidic device preparation, Sylgard 184 Silicone Elastomer Kit (PDMS) was purchased from Dow Corning. Ultra-pure water was obtained from a ultrapure filtration system (Thermo Fisher). All other chemicals were purchased from Sigma-Aldrich. In this manuscript, the buffer composition is always made of 100 mM KCl (potassium chloride).

3D-Chip Fabrication: Molds were designed on computer-aided software (AutoCAD). The design consisted of one straight bottom channel created by photolithography, which was connected to a micro-machined upper cone aligned at the middle of the channel (cf. Figure 1). The channel dimensions were set to $3\text{ cm} \times 500\ \mu\text{m} \times 100\ \mu\text{m}$ (length \times width \times height). The upper cone dimensions were $500\ \mu\text{m} \times 2\ \text{mm}$ (diameter \times height). For producing the bottom channel, the following steps were realized. First, the 2 inch silicon wafer was cleaned by acetone and ethanol, rinsed with deionized water, and then baked on a hot plate at $95\ ^\circ\text{C}$ for 5 min to have a clean and uniform baseline for photoresist coating. The spinning speed and the time of the spin coater were determined to end up with a final coating thickness of $100\ \mu\text{m}$ on the substrate that matches the desired channel height: 2 g of SU-8 was put on the silicon wafer and placed on the spin coater. Rotation speed was set to 500 rpm at an acceleration of $100\ \text{rpm s}^{-1}$ for 20 s, then 1500 rpm at $300\ \text{rpm s}^{-1}$ for 60 s to cover the entire surface uniformly with photoresist. Prior to UV exposure, the photoresist was pre-baked for 15 min at $65\ ^\circ\text{C}$ and then soft baked for 45 min at $95\ ^\circ\text{C}$. To prepare the photoresist coated silicon wafer for UV exposure, a transparent mask with the pattern of the desired bottom channel was placed on it. Afterward, the photoresist-coated sample was exposed through the

photomask to UV light with a wavelength of 400 nm with an intensity of $15\ \text{mW cm}^{-2}$ for 20 s. Following that, post exposure step was done by baking the photoresist at $65\ ^\circ\text{C}$ for 1 min and then $95\ ^\circ\text{C}$ for 5 min to obtain the selective cross-linking. Then, the substrate was immersed in developer solution and gently shaken for 10 min to solve the non-exposed areas properly. As the last step, the substrate was rinsed with acetone, ethanol, and distilled water.

Subsequently, the produced bottom channel and the micro-machined cone were combined to form a 3D negative mold for the replication with PDMS. For that, the micromachined 3D cone was carefully aligned at the middle of the channel and kept in ultimate contact by placing a weight on top of the cone (Figure 1A). After setting up the mold, PDMS (Sylgard 184 – Dow Corning) was mixed and degassed for 30 min and poured directly onto the system and cured at $100\ ^\circ\text{C}$ for 2 h. After curing the PDMS, the cone was carefully removed from the PDMS microchip and the cured PDMS was detached from the photolithographically produced mold of the bottom channel. Inlet and outlet holes were punched into the PDMS at the two ends of the bottom channels, and the PDMS microchip was closed with a thin glass cover slip using plasma bonding (Diener electronics). The final device was put on a hot plate at $95\ ^\circ\text{C}$ for 1 h to increase the bonding strength and to restore the hydrophobic properties of the PDMS. The bottom channel was connected to a 1 mL syringe via punched holes to introduce buffer. All other flow controls were achieved using the access from the upper cone.

Horizontal Free-Standing Lipid Bilayer Formation: All used lipid–oil mixtures were prepared with a concentration of $5\ \text{mg mL}^{-1}$ in squalene oil. The lipids were mixed in squalene via magnetic stirring, and let at $45\ ^\circ\text{C}$ for 3–4 h until completely dissolved.

The free-standing bilayer formation method was based on a variant of the droplet interface bilayer method. First, an aqueous buffer solution was injected into the bottom channel. Please note that the cone was still empty after this step. A first water–oil interface was formed when gently adding a $4\ \mu\text{L}$ drop of $5\ \text{mg mL}^{-1}$ lipid–oil mixture to the upper cone-shaped opening. Subsequently, a second water–oil interface was formed by adding a $10\ \mu\text{L}$ drop of buffer from top into the same cone-shaped opening. As the lipid molecules were amphiphilic, they were similar to a surfactant and covered each water–oil interface. The thickness of this water–oil–water sandwich right after formation was approximately a few ten micrometers. As the PDMS chip was porous, it drained the oil phase separating the two buffer phases, and eventually brought the two lipid monolayers in contact to form a lipid bilayer. The complete adsorption of squalene by PDMS took between 10 min and 2 h depending on the volume of lipid–oil mixture that was introduced to the system. During the absorption of oil, the lipid–oil sandwich became thinner and the lipid bilayer formation started to be visible by the observation of a circle at the middle of the aperture.

Thus, the general principle to successfully make free-standing membranes is to start from two monolayers separated by oil and subsequently drain the oil so that the monolayers contact and form a bilayer. During this process, the drainage phase leaves an annulus of oil and possibly the presence of an oil film between the two lipid monolayers. To significantly reduce the amount of residual oil, Malmstadt et al.^[44] introduced the principle of automated lipid bilayer formation, that is, without any external triggering, in poly(dimethylsiloxane) (PDMS) chip by spontaneous selective solvent extraction. Such solvent extraction by spontaneous swelling of PDMS has been studied in great detail by Whitesides et al.^[9]

Patch-Clamp: Ag/AgCl electrodes were prepared by inserting an electrode in a borosilicate glass pipette (outer diameter 1.5 mm, inner diameter 0.86 mm, VWR) containing an electrolyte agarose solution. The electrodes were carefully introduced into the buffer compartment of the Sylgard 184 device using a micro-manipulator. The lipid membrane conductance was measured using the standard function provided by a patch clamp amplifier (EPC 10 USB, HekaElectronics). For that, a 10 mV sinusoidal wave with a frequency of 20 kHz was used as an excitation signal.

Epifluorescence Microscopy: The experimental setup used for these measurements was an inverted microscope with a motorized focus

system (Axio Observer Z1, Zeiss). The fluorescent sample was excited through the same objective used for image recording by a green laser ($\lambda = 532$ nm, pulsed DPSS, 2.72 W, LaVision), or a blue laser ($\lambda = 473$ nm, pulsed DPSS, 1.5 W, LaVision) and recorded by a sensitive camera (Imager Pro X 2M CCD Camera–LaVision) coupled with the microscope by a camera adapter (Zeiss).

Confocal Microscopy and FRAP: Confocal images were acquired with an inverted microscope (Nikon Ti-Eclipse) with the light source of Intensilight Epi-fluorescence illuminator. The confocal microscope was equipped with a Yokogawa spinning disk head (CSU-W1; Andor Technology) and a fluorescence recovery after photo-bleaching (FRAPPA; Andor Technology) module. Confocal imaging was conducted using excitation wavelengths of 481 nm (for BODIPY 493/503) and 561 nm (for RhodPE 560/583, Atto647NPE 643/665) to distinguish the bilayer area and lipid droplets, respectively. The used emission filters have the wavelengths/bandwidths of 525/30 nm, 607/36 nm and 685/40 nm, respectively. For the FRAP experiments, a pinhole size of 50 μm was used with 40 \times oil objective having a working distance of 220 micrometer. Prior to bleaching, a circular stimulation area with diameter of 50 micrometer was selected inside the bilayer. Fluorescence imaging was performed for 20 s for each individual experiment. Then, bleaching was performed by increasing the laser power on the stimulation area to the maximum laser power for 20 s, including 10 loops and repeated for three times. During the recovery, image acquisition was continued for at least 2 min to be able to observe all the changes after recovery. The z-stacks were in principle achieved by incremental stepping through the bilayer using the focal drive. Imaging was performed by using two different wavelengths of 488 nm, 561 nm and 647 nm with the same 40 \times objective by considering the z-step of the objective, which was 0.3 μm . After capturing the images for both wavelengths, all images were processed by ImageJ-Fiji to obtain 3D images.

Purification of Recombinant S-UBXD8₇₁₋₁₃₂-Atto488-130C-6HIS: The UBXD8 amino acids 71-132, comprising the hydrophobic hairpin domain, were expressed as a fusion protein consisting of an N-terminal GST-tag followed by a PreScission Protease cleavage site and an S-peptide-tag before the UBXD8 peptide sequence, which also contains a single cysteine at position 130 allowing covalent attachment of a maleimide-fluorophore. C-terminally, a hexahistidine-tag was added. Protein synthesis was induced in *E. coli* BL21 pRARE with 0.5 mM IPTG at an $\text{OD}_{600\text{nm}}$ of 1 for 1 h at 37 °C. Pelleted cells were resuspended in 50 mM TRIS/HCl pH 8.0, 0.5 mM EDTA, 1 mM MgCl_2 including protease inhibitors (Pepstatin A, Chymostatin, Antipain, 0.02 mg mL^{-1} each), 0.16 mg mL^{-1} lysozyme and 0.1 U μL^{-1} Benzozonase. After 45 min incubation at 30 °C and 5 min sonication (Bandelin Sonotrode VS70T set at cycle 7, 50%), the lysate was centrifuged at 17 000 $\times g$ for 1 h at 4 °C. The pellet was resuspended in 50 mM HEPES pH 8.0, 300 mM NaCl, 0.4 mM EDTA, protease inhibitors, sonicated for 2 min (cycle 7, 50 %), supplemented with 1% w/v DDM and rotated at 4 °C overnight. After centrifugation at 17 000 $\times g$ for 1 h at 4 °C, the supernatant was diluted with 50 mM HEPES pH 8.0, 300 mM NaCl to 0.5% w/v DDM and incubated with GSH-Sepharose beads (Cytiva) for 1 h at 4 °C. After washing with 50 mM HEPES pH 8.0, 300 mM NaCl, 0.5 % w/v DDM, the protein was eluted by incubation with PreScission Protease in 50 mM TRIS/HCl pH7, 150 mM NaCl, 1 mM EDTA, 1 mM DTT, 0.5% DDM w/v. The eluate was supplemented with 20 mM imidazole and added to Ni NTA Agarose beads (Qiagen). After washing with 50 mM TRIS/HCl pH 8.0, 300 mM NaCl, 20 mM imidazole, 2 mM beta-mercaptoethanol, 0.2 % w/v DDM, proteins were eluted with 300 mM imidazole in the same buffer. Buffer was exchanged to 50 mM HEPES pH 7.0, 150 mM NaCl, 1 mM EDTA, 5 % v/v glycerol, 0.2 % w/v DDM using gel filtration and the protein labeled with 0.05 mM ATTO488 maleimide (Atto-Tec AD 488-45). Unincorporated label was removed by gel filtration.

Preparation of Liposomes: After mixing POPC and DOPS (Avanti Polar Lipids) dissolved in chloroform in a 9:1 ratio, the lipids were dried under a stream of nitrogen. Residual chloroform was removed under vacuum in a desiccator for 1 h at room temperature. The dried lipids were resuspended in RB (20 mM HEPES pH7.4, 150 mM NaCl,

5 % (v/v) glycerol) by shaking for 30 min at 60 °C and 1200 rpm and sonication for 20 min at 60 °C in a water bath.

Reconstitution of S-UBXD8₇₁₋₁₃₂-Atto488-130C-6HIS into Proteo-Liposomes: For protein (S-UBXD8₇₁₋₁₃₂-Atto488-130C-6HIS) reconstitution in liposomes, POPC/DOPS (9:1) liposomes in buffer RB were solubilized in 24 mM DDM (ROTH), mixed with the purified protein and incubated with fresh Bio-Beads SM-2 (BioRad) twice for 2 h at room temperature for detergent removal. To separate proteo-liposomes from non-reconstituted protein, the supernatant was supplemented with 0.24 M sucrose and 50 % v/v Optiprep (Sigma-Aldrich) and fractionated on a density step gradient (50 % Optiprep and 0.24 M sucrose in RB, 30 % Optiprep and 0.24 M sucrose in RB, RB only) by centrifugation in a swinging bucket rotor at 230 335 $\times g$ for 3 h at 4 °C. Fractions were collected from top to bottom and analyzed by Western Blotting and dynamic light scattering to identify the proteo-liposome-containing fraction, which was then used for the generation of proteo-LDs.

LDs and Proteo-LDs Formation: For the preparation of lipid droplets in bulk, all lipids and BODIPY (493/503) were used from their chloroform stock solutions, which all had a concentration of 10 mg mL^{-1} . A chloroform droplet of 200 μL volume, which is 1 mg in total, with the lipid composition DOPC:DOPE:Triolein:BODIPY (35:35:28:2) was deposited and dried on a glass falcon (1 h under vacuum). Afterward, 1 mL of 0.1 M NaCl buffer was added and sonicated for 5 min to obtain a dense solution of lipid–oil droplets in water. Using microscopy, the average size of these lipid droplets could be measured to be around 5 μm . The solution was diluted with the buffer to the ratio of 1:4 vol/vol just before the experiment to decrease the coalescence rate of the formed lipid droplets. The lipid droplets in bulk were stable for the duration of all kinds of experiments conducted in the course of this work and used for the insertion experiments by directly adding them to the system after bilayer formation.

To prepare the proteo-LDs, first a bi-phase of Triolein and buffer was created. For this aim, 10 μL of triolein (from 10 mg mL^{-1} stock solution) was added to an empty vial and the chloroform was evaporated completely in a vacuum desiccator. After that, 180 μL of the buffer solution was added to the triolein. Here, the same buffer as for the proteo-liposome solution was used. Consequently, 20 μL of ready-to-use proteo-liposomes were combined by this bi-phase. After storing this solution overnight at 4 °C, it was sonicated until achieving proteo-LDs with a size of 15 μm . These dispersions of proteo-LDs were directly used in the experiments.

Interfacial Tension Measurements: The interfacial tension was determined by the pending drop method using the contact angle measurement device OCA 25 (DataPhysics, Germany). For this method, a droplet with a defined volume of the denser fluid, here the buffer solution ($\rho_{\text{buffer}} = 0.998$ g cm^{-3}), is created in a transparent cuvette filled by the fluid with lower density, here the squalene-phospholipid mixture ($\rho_{\text{oil}} = 0.858$ g cm^{-3}). While gravity drags the droplet down, buoyancy and surface forces keep the droplet in place. The interfacial tension can then be determined based on a Young-Laplace fitting by imaging the vertical cross-section of the droplet and extracting a geometry factor to estimate the surface force which is automatically accomplished by the software SCA 20. The interfacial tension was determined when the whole water-oil interface is decorated with lipid-molecules and before the droplet detached from the needle. Therefore, the droplet volume defines an upper limit for the interfacial tension and was set to (2.0 \pm 0.5) μL , which guaranteed a sufficient contour length for a proper fit. An upper approximation allowed to compare the relative difference for slight variations in the chemical composition of the mixture. From the values of the surface tension obtained from pendant drop measurements, and the bilayer contact angle 2θ obtained from optical micrographs, the bilayer tension could be calculated using the Young equation

$$\Gamma = 2\gamma \cos(\theta) \quad (10)$$

Molecular Dynamics Simulations: To test whether different lipid types were preferentially located at different regions of the LD, MD simulations were used. The simulation was carried out with the Gromacs simulation

software, version 2020.4.^[45] Molecular interactions were described with the Martini 2.0 coarse-grained force field.^[41] Neighbor lists were updated with the Verlet algorithm. Lennard–Jones and Coulomb interactions were truncated at 1.1 nm. The temperature was controlled at 310 K using velocity rescaling using three separate coupling groups for i) the neutral lipids, ii) phospholipids, and iii) solvent ($\tau = 1.0$ ps).^[46] A constant surface tension of 50 bar nm was applied in the membrane plane, while maintaining a pressure of 1 bar along z direction with the Berendsen barostat ($\tau = 6$ ps).^[47] Constraints were solved with LINCS.^[48] The integration time step was set to 20 fs.

The CG simulations were set up as follows (Figure 6). Lipid bilayers were first set up with the Insane software,^[49] solvated with CG water, neutralized with sodium beads, and fully equilibrated. The bilayer system contained 5000 lipids in total composed of DOPC:DOPE:DOPS with a ratio of 50:40:10, 126 478 water beads, and 244 sodium beads. The two monolayers were moved apart along the z-direction (membrane normal) to form a gap of 5.8 nm between the monolayers. A cylindrical volume between the monolayers was filled with 529 triacylglycerol (TAG) lipids, where the cylinder radius was taken as 8 nm and the cylinder axis was parallel to the z axis. The lateral diffusion of TAG lipids was restrained using cylindrical flat-bottomed potential with a radius of 8 nm and a force constant of 50 kJ mol⁻¹ nm⁻². This setup imposed an LD radius of approximately 8 nm and, thereby, the formation of well-defined kink between the bilayer and the two monolayers. However, the shape of the LD was not controlled only by the force field but instead by the number of TAG lipid together with the imposed LD radius. The system was simulated for 10 ns with pressure coupling along z direction while keeping the simulation box area in the membrane plane constant, allowing the system to close the gap between the two monolayers and, thereby, to form the LD. Henceforth, the system was equilibrated for another 10 ns with constant surface tension in the membrane plane as described above. From the final frame, a production simulation of 9.93 μ s was carried out. The first 0.5 μ s of the simulation was omitted from analysis for equilibration.

The mean first passage times (Table 2) for lipid diffusion from the bilayer onto the LD surface or vice versa were computed by tracking the lateral distance r_{lat} (projected onto the x-y plane) of each phosphate bead from the center of mass of the LD. A transition from $r_{\text{lat}} < 5$ nm to $r_{\text{lat}} > 13$ nm was defined as a successful LD-to-bilayer transition. Inversely, a transition from $r_{\text{lat}} > 13$ nm to $r_{\text{lat}} < 5$ nm was defined as a successful bilayer-to-LD transition. The same definition was used for a pure-bilayer simulation, except that r_{lat} was taken as the lateral center of the simulation box. A picture of MD simulation is provided in Figure 6.

Supporting Information

Supporting Information is available from the Wiley Online Library or from the author.

Acknowledgements

Financial support is acknowledged by the Deutsche Forschungsgemeinschaft (DFG), SFB1027 to J.S.H (project B7), B.S. (project C9), and to R.S. and J-B.F. (project B4).

Open access funding enabled and organized by Projekt DEAL.

Conflict of Interest

The authors declare no conflict of interest.

Data Availability Statement

The data that support the findings of this study are available from the corresponding author upon reasonable request.

Keywords

lipid bilayers, lipid diffusion, lipid droplets, monotopic membrane proteins, phospholipid monolayers, wetting

Received: October 26, 2021

Revised: December 9, 2021

Published online:

- [1] M. A. Welte, A. P. Gould, *Biochim. Biophys. Acta, Mol. Cell Biol. Lipids* **2017**, *1862*, 1260.
- [2] Y. Guo, T. C. Walther, M. Rao, N. Stuurman, G. Goshima, K. Terayama, J. S. Wong, R. D. Vale, P. Walter, R. V. Farese, *Nature* **2008**, *453*, 657.
- [3] T. C. Walther, J. Chung, R. V. Farese, *Ann. Rev. Cell Dev. Biol.* **2017**, *33*, 491.
- [4] J. A. Olzmann, P. Carvalho, *Nat. Rev. Mol. Cell Biol.* **2019**, *20*, 137.
- [5] H. Khandelia, L. Duelund, K. I. Pakkanen, J. H. Ipsen, *PLoS ONE* **2010**, *5*, e12811.
- [6] M. J. Greenall, C. M. Marques, *Soft Matter* **2012**, *8*, 3308.
- [7] V. Zoni, V. Nieto, L. J. Endter, H. J. Risselada, L. Monticelli, S. Vanni, *Front. Mol. Biosci.* **2019**, *6*, 2017.
- [8] A. Masedunskas, Y. Chen, R. Stussman, R. Weigert, I. H. Mather, *MBoC* **2017**, *28*, 935.
- [9] K. D. Chapman, J. M. Dyer, R. T. Mullen, *J. Lipid Res.* **2012**, *53*, 215.
- [10] V. Choudhary, N. Ojha, A. Golden, W. A. Prinz, *J. Cell Biol.* **2015**, *211*, 261.
- [11] R. Dhiman, S. Caesar, A. R. Thiam, B. Schrul, *Semin. Cell Dev. Biol.* **2020**, *108*, 4.
- [12] K. Bersuker, J. A. Olzmann, *Biochim. Biophys. Acta* **2017**, *1862*, 1166.
- [13] A. L. S. Cruz, E. d. A. Barreto, N. P. B. Fazolini, J. P. B. Viola, P. T. Bozza, *Cell Death Dis.* **2020**, *11*, 105.
- [14] T. Fujimoto, R. G. Parton, *Cold Spring Harb. Perspect. Biol.* **2011**, *3*, 3.
- [15] R. Bartz, W.-H. Li, B. Venables, J. K. Zehmer, M. R. Roth, R. Weltri, R. G. W. Anderson, P. Liu, K. D. Chapman, *J. Lipid Res.* **2007**, *48*, 837.
- [16] K. Tauchi-Sato, S. Ozeki, T. Houjou, R. Taguchi, T. Fujimoto, *J. Biol. Chem.* **2002**, *277*, 44507.
- [17] P. J. Horn, N. R. Ledbetter, C. N. James, W. D. Hoffman, C. R. Case, G. F. Verbeck, K. D. Chapman, *J. Biol. Chem.* **2011**, *286*, 3298.
- [18] G. Onal, O. Kutlu, D. Gozuacik, S. Dokmeci Emre, *Lipids Health Dis.* **2017**, *16*, 128.
- [19] T. Fujii, *Microelectron. Eng.* **2002**, *61-62*, 907.
- [20] P. Heo, S. Ramakrishnan, J. Coleman, J. E. Rothman, J.-B. Fleury, F. Pincet, *Small* **2019**, *15*, 1900725.
- [21] H. Kusumaatmaja, R. Lipowsky, *Soft Matter* **2011**, *7*, 6914.
- [22] B. Winckler, P. Forscher, I. Mellman, *Nature* **1999**, *397*, 698.
- [23] H. Tawfik, S. Puza, R. Seemann, J.-B. Fleury, *Front. Cell Dev. Biol.* **2020**, *8*, 531229.
- [24] J.-B. Fleury, M. Werner, X. L. Guével, V. A. Baulin, *J. Colloid Interface Sci.* **2021**, *603*, 550.
- [25] K. Triantafilou, M. Triantafilou, S. Ladha, A. Mackie, R. L. Dedrick, N. Fernandez, R. Cherry, *J. Cell Sci.* **2001**, *114*, 2535.
- [26] M. Garten, L. D. Mosgaard, T. Bornschlöggl, S. Dieudonné, P. Bassereau, G. E. S. Toombes, *Proc. Natl. Acad. Sci. U. S. A.* **2017**, *114*, 328.
- [27] L. Fouillen, L. Maneta-Peyret, P. Moreau, *Methods Mol. Biol.* **2018**, *1691*, 125.
- [28] T. K. Fam, A. S. Klymchenko, M. Collot, *Materials (Basel)* **2018**, *11*, 9.
- [29] P. A. Ferrari, S. Goldstein, J. L. Lebowitz, in: *Statistical Physics and Dynamical Systems: Rigorous Results* (Eds: J. Fritz, A. Jaffe, D. Szász), Progress in Physics, Birkhäuser, Boston, MA **1985**, pp. 405–441.

- [30] V. Choudhary, G. Golani, A. S. Joshi, S. Cottier, R. Schneider, W. A. Prinz, M. M. Kozlov, *Curr. Biol.* **2018**, *28*, 915.
- [31] L. V. Chernomordik, M. M. Kozlov, *Nat. Struct. Mol. Biol.* **2008**, *15*, 675.
- [32] C. S. Poojari, K. C. Scherer, J. S. Hub, Free energies of stalk formation in the lipidomics era, Technical report, **2021**, <https://www.biorxiv.org/content/10.1101/2021.06.02.446700v1>, Company: Cold Spring Harbor Laboratory Distributor: Cold Spring Harbor Laboratory Label: Cold Spring Harbor Laboratory Section: New Results Type: article.
- [33] P. G. de Gennes, *Rev. Mod. Phys.* **1985**, *57*, 827.
- [34] N. Khangholi, R. Seemann, J.-B. Fleury, *Biomicrofluidics* **2020**, *14*, 024117.
- [35] A. Chorlay, A. R. Thiam, *Biophys. J.* **2018**, *114*, 631.
- [36] A. Chorlay, L. Monticelli, J. V. Ferreira, K. B. M'barek, D. Ajjaji, S. Wang, E. Johnson, R. Beck, M. Omrane, M. Beller, P. Carvalho, A. R. Thiam, *Develop. Cell* **2019**, *50*, 25.
- [37] T. Takei, T. Yaguchi, T. Fujii, T. Nomoto, T. Toyota, M. Fujinami, *Soft Matter* **2015**, *11*, 8641.
- [38] D. M. Soumpasis, *Biophys. J.* **1983**, *41*, 95.
- [39] T. Wang, C. Ingram, J. C. Weisshaar, *Langmuir* **2010**, *26*, 11157.
- [40] M. Przybylo, J. Sýkora, J. Humpolickova, A. Benda, A. Zan, M. Hof, *Langmuir* **2006**, *22*, 9096.
- [41] S. J. Marrink, H. J. Risselada, S. Yefimov, D. P. Tieleman, A. H. de Vries, *J. Phys. Chem. B* **2007**, *111*, 7812.
- [42] V. Zoni, R. Khaddaj, P. Campomanes, A. R. Thiam, R. Schneider, S. Vanni, *eLife* **2021**, *10*, e62886.
- [43] L. Caillon, V. Nieto, P. Gehan, M. Omrane, N. Rodriguez, L. Monticelli, A. R. Thiam, *Nat. Comm.* **2020**, *11*, 3944.
- [44] N. Malmstadt, M. A. Nash, R. F. Purnell, J. J. Schmidt, *Nano Lett.* **2006**, *6*, 1961.
- [45] M. J. Abraham, T. Murtola, R. Schulz, S. Páll, J. C. Smith, B. Hess, E. Lindahl, *SoftwareX* **2015**, *1-2*, 19.
- [46] G. Bussi, D. Donadio, M. Parrinello, *J. Chem. Phys.* **2007**, *126*, 014101.
- [47] H. J. C. Berendsen, J. P. M. Postma, W. F. van Gunsteren, A. DiNola, J. R. Haak, *J. Chem. Phys.* **1984**, *81*, 3684.
- [48] B. Hess, *J. Chem. Theory Comput.* **2008**, *4*, 116.
- [49] T. A. Wassenaar, H. I. Ingólfsson, R. A. Böckmann, D. P. Tieleman, S. J. Marrink, *J. Chem. Theory Comput.* **2015**, *11*, 2144.